HEALTH AND MEDICINE

Highly bioactive zeolitic imidazolate framework-8–capped nanotherapeutics for efficient reversal of reperfusion-induced injury in ischemic stroke

Lizhen He*, Guanning Huang*, Hongxing Liu, Chengcheng Sang, Xinxin Liu, Tianfeng Chen†

Rational design of potent antioxidative agent with high biocompatibility is urgently needed to treat ischemic reperfusion-induced ROS-mediated cerebrovascular and neural injury during ischemia strokes. Here, we demonstrate an in situ synthetic strategy of bioactive zeolitic imidazolate framework-8–capped ceria nanoparticles (CeO_2@ZIF-8 NPs) to achieve enhanced catalytic and antioxidative activities and improved stroke therapeutic efficacy. This nanosystem exhibits prolonged blood circulation time, reduced clearance rate, improved BBB penetration ability, and enhanced brain accumulation, where it effectively inhibits the lipid peroxidation in brain tissues in middle cerebral artery occlusion mice and reduces the oxidative damage and apoptosis of neurons in brain tissue. CeO_2@ZIF-8 also suppresses inflammation- and immune response–induced injury by suppressing the activation of astrocytes and secretion of proinflammatory cytokines, thus achieving satisfactory prevention and treatment in neuroprotective therapy. This study also sheds light on the neuroprotective action mechanisms of ZIF-8–capped nanomedicine against reperfusion-induced injury in ischemic stroke.

INTRODUCTION

Ischemic stroke, accounting for about 85% of strokes and having increasing mortality and long-term disability rates, is one of the most serious public health problems (*1*, *2*). In the process of reperfusion, blood flow restoration in the ischemic brain not only improves the oxygen supply but also induces the overproduction of reactive oxygen species (ROS), including superoxide anion ($^{\bullet}O_2^-$), hydrogen peroxide (H_2O_2), and hydroxyl radical ($^{\bullet}OH$), to cause the secondary injury in cerebrovascular system and neural networks (*3*, *4*). The excessive ROS generation can mediate inflammation and immune response by stimulating the expression of cytokines and adhesion molecules, ultimately causing further injury by inflammation, finally leading to ischemia-reperfusion injury (*5*, *6*). Edaravone-based neuroprotective therapy is the main strategy for the treatment of ischemic stroke by eliminating the free radicals and suppressing oxidative stress (*7*–*9*). However, its clinical application is limited by the low bioavailability, short half-life, inefficient penetration across the blood-brain barrier (BBB), and the side effects to kidney and liver functions. Therefore, the design and development of agents with potent ROS scavenging activity and desirable physicochemical property for the treatment of ischemia strokes is urgently needed.

Nanotechnology-mediated antioxidative therapy has been proven as a promising method for the treatment of the diseases induced by oxidative damage (*10*–*13*). Until now, various nanoantioxidants, such as melanin (*14*), carbon, platinum, ceria (CeO_2), manganese (*15*), and magnetite/ceria nanoparticle (NP) (*16*), have been designed to achieve efficient treatments for stroke and other chronic diseases. Different nanosystems have been synthesized to mediate intracellular ROS to achieve therapeutic use (*17*, *18*). Among these nanomaterials, CeO_2 NPs have attracted great interest owing to their high antioxidant activity and recyclable ROS scavenging ability (*19*). Because of the fluorite lattice structure, under physiological conditions, CeO_2 NPs could easily lose oxygen or get electrons, resulting in the formation of oxygen vacancy and lowered valence states, and the electron transfer between Ce(III) and Ce(IV) endows it with potent antioxidant activity and repetitive ROS elimination ability (*20*). For instance, Kim *et al.* (*21*) have reported that ceria NPs can protect brain tissue against oxidative damage during ischemic stroke. Bao *et al.* (*22*) have designed and synthesized effective stroke treatment agents based on monodisperse CeO_2 NPs with simultaneous BBB crossing and protection activity by loading with edaravone. In addition, neutrophil and red blood cell membranes were also used to decorate nanovesicles for ischemic stroke therapy (*23*, *24*). However, the further clinical development of these stroke treatment NPs is limited by the short vascular circulation time, easy interparticle aggregation, and undesirable occurrence of direct catalytic reaction on exposed active sites. Therefore, the construction of a stable and biocompatible shell encapsulation of the chemically active CeO_2 NPs is a good way to overcome these drawbacks.

As unique porous materials, metal-organic frameworks (MOFs) have been recognized as potential encapsulation shell and drug carriers for biomedical applications due to their high porosity, large surface areas, tunable functionality, and well-defined pore structures (*25*, *26*). Zeolitic imidazolate framework–8 (ZIF-8) is one of the most promising representatives of MOFs built from zinc ions and 2-methylimidazolate (2-MI), thus exhibiting nontoxic and biocompatible advantages (*27*). Nanoscale ZIF-8 was stable under physiological conditions and could decompose under acidic environments because of protonation effect (*28*), such as tumor tissues and acidic organelles, thus making it highly suitable for constructing pH-responsive drug delivery systems. ZIF materials have also been applied in encapsulation of small-molecule drugs, larger drug molecules, enzymes, and even NPs, including numerous noble metal NPs such as Pt, Pd, and Au, to develop core/shell nanocomposites with new functions and biological applications (*25*, *29*–*31*). The encapsulation with ZIF could modify the surface properties of NPs and prevent the aggregation, thus enhancing the stability under physiological conditions. Moreover, the cavity and porous structure could endow the materials with size-sieving behavior to regulate the diffusion and reaction process

The First Affiliated Hospital, and Department of Chemistry, Jinan University, Guangzhou 510632, China.
*These authors contributed equally to this work.
†Corresponding author. Email: tchentf@jnu.edu.cn

of large molecules to increase reaction selectivity (*25*). Inspired by this, it is possible that the unique porous and bioresponsive properties of ZIF-8 can help to protect the exposed active sites in CeO_2 NPs and to regulate the controlled release of active components.

Therefore, in this study, we explored a new in situ synthesis strategy of ZIF-8–capped CeO_2 NPs (CeO_2@ZIF-8) with enhanced catalytic and antioxidative activities. This smart design can overcome the drawbacks of CeO_2 NPs and achieve the following advantages: (i) The surface ZIF-8 acts as peroxidase to maintain the antioxidant activity in the presence of excessive H_2O_2 or other oxidants, which can absorb H_2O_2 and destroy the O—O bond to disintegrate H_2O_2. (ii) The ZIF-8 frame growing on the outer layer of CeO_2 NPs controls the size, shape, and surface charge of CeO_2 core to make it more suitable for biological application. (iii) The decomposition of ZIF-8 results in the release of active components, which synergistically enhance the stroke therapeutic efficacy of CeO_2. As expected, CeO_2@ZIF-8 NPs exhibit effective ROS scavenging in vitro and protect PC12 neuronal cells from free radical–induced apoptosis. ZIF-8 encapsulation can also effectively prolong the blood circulation time of CeO_2, reduce the clearance rate, improve the penetration across BBB, and enhance its accumulation in brain tissue. As a result, this nanosystem effectively inhibits the lipid peroxidation in brain tissues of middle cerebral artery occlusion (MCAO) model mice, reduces the oxidative damage and apoptosis of neurons in brain tissue, and suppresses the inflammation- and immune response–induced injury, thus achieving satisfactory prevention and treatment in neuroprotective therapy during ischemic stroke with high safety. Together, this study not only provides a new in situ synthetic approach of synergistic nanotherapeutics by using ZIF as bioactive surface decoration and CeO_2 NPs as functional core but also sheds light on the neuroprotective application mechanisms against reperfusion-induced injury in ischemic stroke.

RESULTS AND DISCUSSION

Rational design and in situ synthesis of ZIF-capped CeO_2 NPs

In this study, we have rationally designed and synthesized ZIF-8–capped CeO_2 NPs (CeO_2@ZIF-8 NPs; Fig. 1A) to achieve enhanced catalytic and antioxidative activities. In this nanosystem, ZIF-8 encapsulation can control size and surface charge of CeO_2 core to make it more suitable for biological application. First, CeO_2 nanopolyhedra were successfully created through a facile hydrothermal method with a size of ~20 ± 5 nm (fig. S1, A and B). ZIF-8 with a nanoscale at ~140 nm (Fig. 1B) was synthesized according to previous procedures with modification. Here, we also explored a new in situ synthesis method of CeO_2@ZIF-8 composite nanomaterials, which make the ZIF-8 frame grow on the outer layer of CeO_2. The synthesized CeO_2@ZIF-8 nanomaterials appear as highly monodisperse particles with a diameter of ~240 nm (Fig. 1C), and CeO_2 is distributed within the framework of ZIF-8, as shown in the elemental mapping of Ce and Zn (Fig. 1, D and E). As examined by a laser particle size and zeta potential analyzer, the average particle sizes of CeO_2, ZIF-8, and CeO_2@ZIF-8 are ~88.3, ~168, and ~275 nm, respectively, and the zeta potentials are ~32.4, ~4.9, and ~10.5 eV, respectively (fig. S1, C and D). Furthermore, CeO_2@ZIF-8 exhibited the highest stability in aqueous solution and Dulbecco's modified Eagle's medium (DMEM) (fig. S1E). We also used transmission electron microscopy (TEM) to investigate the morphology of CeO_2@ZIF-8 in H_2O, DMEM, and phosphate-buffered saline (PBS) for 24 and 48 hours. As shown in fig. S1F, CeO_2@ZIF-8 was slightly degraded in H_2O for 24 and 48 hours. However, it was unstable in the PBS (pH 7.4) buffer and could slowly decompose during the incubation. In contrast, in DMEM with 10% fetal bovine serum (FBS), CeO_2@ZIF-8 was kept stable even after 48-hour incubation, which could be due to the formation of protein corona that could protect the nanosystem during blood circulation. X-ray diffraction (XRD) pattern showed that, after growth in the framework of ZIF-8, CeO_2 still has a pure and typical fluorite cubic structure, and the outer layer of ZIF-8 retains its crystal structure (Fig. 1F). Furthermore, CeO_2@ZIF-8 exhibits the same characteristic absorption peak with pure CeO_2 in ultraviolet-visible (UV-vis) spectra, indicating the presence of CeO_2 in ZIF-8 (Fig. 1G). Raman spectra of CeO_2@ZIF-8 show the characteristic absorption peaks of CeO_2 and ZIF-8, and no new absorption peaks are formed, which indicates that there is no new chemical bond between CeO_2 and ZIF-8 (Fig. 1H). As shown in Fig. 1I, the presence of Ce 3d and Zn 2p peaks in the x-ray photoelectron spectroscopy (XPS) spectrum of CeO_2@ZIF-8 further confirmed the successful synthesized composite nanomaterial with CeO_2 and ZIF-8. The unaltered Zn 2p and Ce 3d spectra of ZIF-8, CeO_2, and CeO_2@ZIF-8 further confirmed that no new chemical bonds were formed between ZIF-8 and CeO_2 (Fig. 1, J and K). Meanwhile, the content ratio of CeO_2 in CeO_2@ZIF-8 composite nanomaterials was ~0.278-mg CeO_2/mg CeO_2@ZIF-8 by inductively coupled plasma mass spectrometry (ICP-MS) analysis. These results confirm the successful synthesis of CeO_2@ZIF-8 NPs.

Enhancement of ROS scavenging by ZIF encapsulation

It is well known that ROS are excessively produced during ischemia-reperfusion in stroke, resulting in damage to the cerebrovascular system and neural networks (*32*, *33*). CeO_2 NPs have been reported as effective free radical scavengers to prevent neuron damage by ROS (*15*, *19*). In this study, we have evaluated the ROS scavenging activity of CeO_2, ZIF-8, and CeO_2@ZIF-8 (Fig. 2A). First, we examined the total antioxidant activities of CeO_2, ZIF-8, and CeO_2@ZIF-8 by ABTS [2,2′-azinobis-(3-ethylbenzothiazoline-6-sulfonate)] free radical scavenging assays. As shown in Fig. 2B and fig. S2 (A to C), CeO_2@ZIF-8 notably inhibits the formation of ABTS free radicals in a time- and dose-dependent manner, suggesting higher antioxidant activity than those of ZIF-8 and CeO_2 nanopolyhedra alone. We then examined the reactions of CeO_2, ZIF-8, and CeO_2@ZIF-8 with H_2O_2 by in situ Raman spectroscopy. As shown in Fig. 2C and fig. S2 (D and E), after adding H_2O_2 onto the surfaces of CeO_2, ZIF-8, and CeO_2@ZIF-8 nanomaterials, the peak of 880 cm^{-1} immediately appeared, and the special peaks of ZIF-8 and CeO_2 disappeared in the Raman spectra of these nanomaterials. The new peak formation may be due to the formation of O—O stretching after adsorption of O_2^{2-} from H_2O_2. Furthermore, as the reaction progresses, the peak of 880 cm^{-1} weakens or even disappears, and the characteristic peak of CeO_2 at 460 cm^{-1} reappears after 40 min, while the special peaks of ZIF-8 did not reappear after reaction with H_2O_2. We then examined the morphological changes of ZIF-8 after reaction with H_2O_2 by TEM. As shown in Fig. 2D, after incubation with 5% H_2O_2 for 3 hours, the ZIF-8 NPs were broken into pieces, and CeO_2@ZIF-8 was cracked to leave CeO_2 nanopolyhedra, indicating that the ZIF-8 NPs can be degraded in the environment of 5% H_2O_2. These results indicate that CeO_2 and CeO_2@ZIF-8 have excellent recyclable antioxidant property to react with H_2O_2 repeatedly due to the presence of CeO_2 nanopolyhedra.

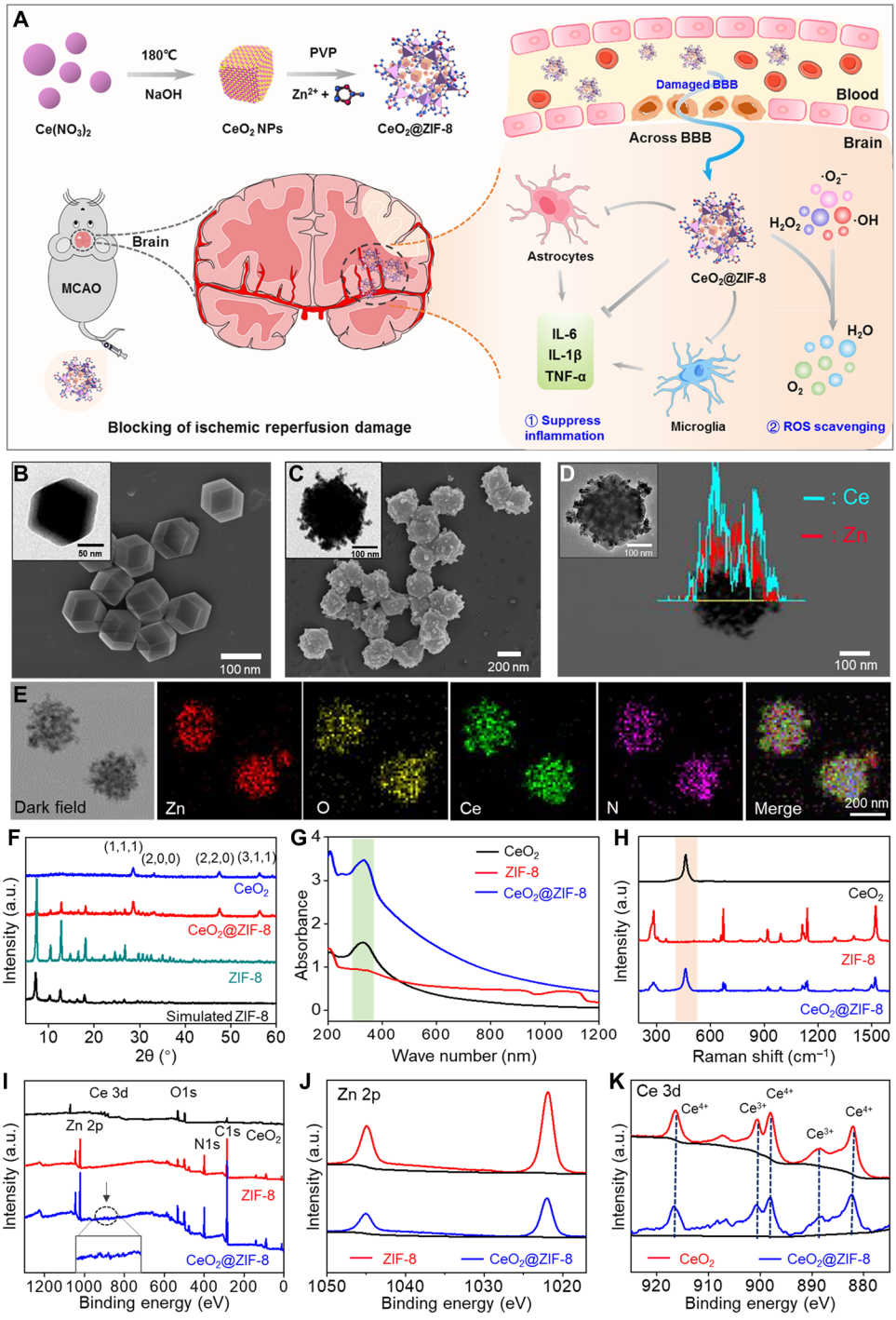

Fig. 1. Structural characterization of CeO_2@ZIF-8 nanomaterials. (**A**) Schematic illustration for in situ synthetic approach of CeO_2@ZIF-8 nanotherapeutics and its neuroprotective application mechanisms against reperfusion-induced injury in ischemic stroke. (**B** and **C**) SEM and TEM images of ZIF-8 (B) and CeO_2@ZIF-8 nanomaterials (C). (**D**) HAADF-STEM (high-angle annular dark-field imaging–scanning TEM) image and linear TEM-EDS (energy-dispersive x-ray spectroscopy) image of CeO_2@ZIF-8. (**E**) Elemental mapping of CeO_2@ZIF-8. XRD pattern (**F**), UV-vis spectra (**G**), Raman spectra (**H**), and XPS spectra (**I**) of CeO_2, ZIF-8, and CeO_2@ZIF-8 nanomaterials. (**J** and **K**) XPS analysis of Zn 2p (J) and Ce 3d (K) spectra of ZIF-8, CeO_2, and CeO_2@ZIF-8 nanomaterials. a.u., arbitrary units.

Furthermore, electron paramagnetic resonance (EPR) spectra were used to examine the •OH scavenging by CeO_2, ZIF-8, and CeO_2@ZIF-8 nanomaterials. The •OH is generated through the Fenton reaction with Fe^{2+}/H_2O_2 system and detected by 5,5′-dimethylpyrroline-1-oxide (DMPO). As shown in Fig. 2E, the EPR spectra of Fenton reaction induce the special signals of DMPO-OH adducts, suggesting the successful generation of •OH. After adding CeO_2, ZIF-8, and CeO_2@ZIF-8 in Fe^{2+}/H_2O_2 system, the signal intensity sharply decreased, especially for CeO_2@ZIF-8, with the same concentration of 15 μg/ml. We then also examined the •OH scavenging activity by

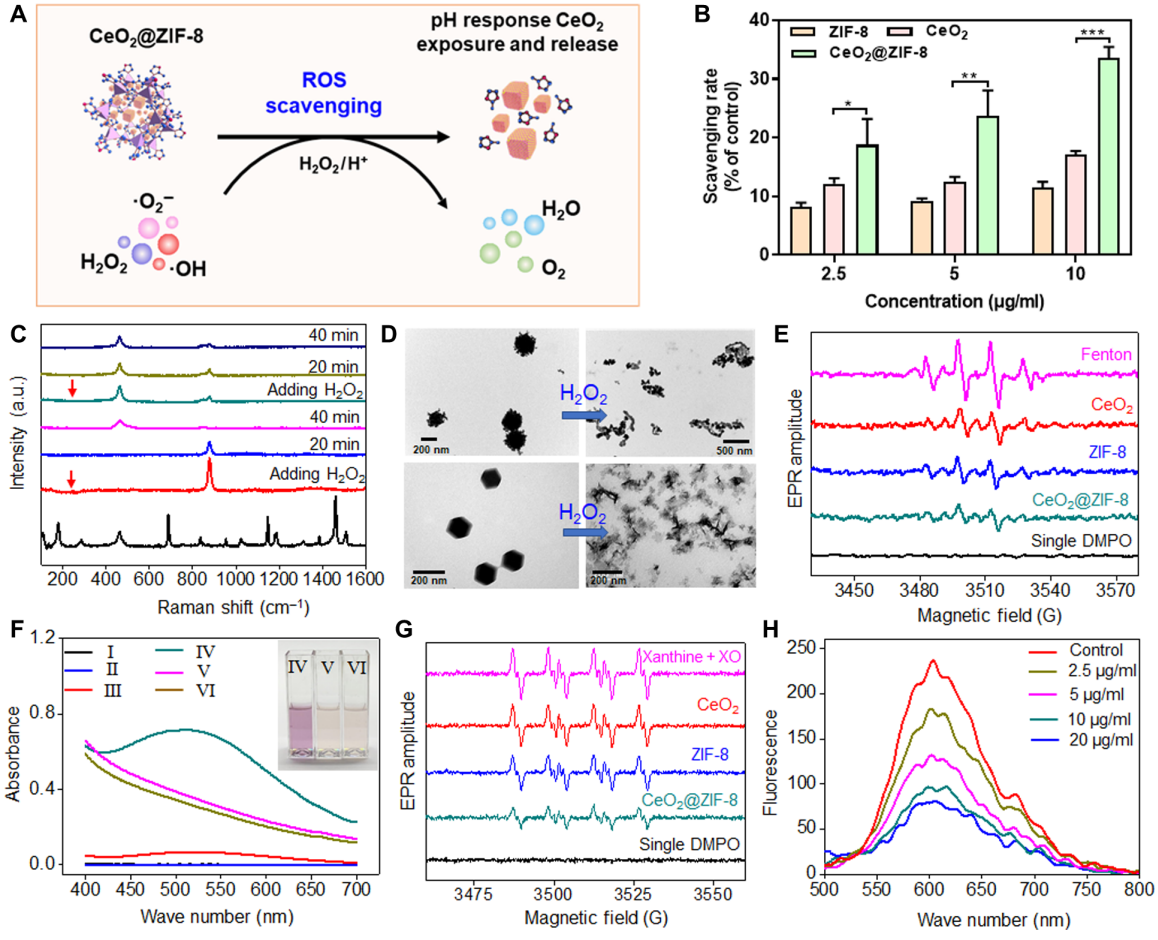

Fig. 2. ROS scavenging by CeO_2@ZIF-8 nanomaterials in vitro. (**A**) Schematic demonstration of ROS scavenging by CeO_2@ZIF-8 nanomaterials in vitro. (**B**) In vitro antioxidant activity of CeO_2, ZIF-8, and CeO_2@ZIF-8 nanomaterials as determined by ABTS free radical scavenging assays. *$P < 0.05$, **$P < 0.01$, and ***$P < 0.001$. (**C**) Raman spectra of CeO_2@ZIF-8 after reaction with H_2O_2 at various time points. (**D**) TEM image of CeO_2@ZIF-8 and ZIF-8 after incubations in aqueous solution with H_2O_2 (5%) for 3 hours. (**E**) EPR spectra analysis of the ˙OH scavenging by CeO_2 (15 μg/ml), ZIF-8, and CeO_2@ZIF-8 nanomaterials. ˙OH was generated by the Fenton reaction with Fe^{2+}/H_2O_2 system and detected by DMPO. (**F**) UV-vis spectra of salicylic acid (SA) after reaction with ˙OH generated by the Fenton reaction with Fe^{2+}/H_2O_2 system for 10 min. I: SA; II: SA + H_2O_2; III: SA + Fe^{2+}; IV: SA + Fe^{2+}/H_2O_2; V: SA + Fe^{2+}/H_2O_2 + CeO_2@ZIF-8 (10 μg/ml); VI: SA + Fe^{2+}/H_2O_2 + CeO_2@ZIF-8 (20 μg/ml). (**G**) EPR spectra analysis of $^{\cdot}O_2^-$ scavenging with CeO_2, ZIF-8, and CeO_2@ZIF-8 nanomaterials (15 μg/ml). $^{\cdot}O_2^-$ was generated by the reaction of xanthine and xanthine oxidase for 30 min and detected by the DHE probe. (**H**) Fluorescence spectra analysis of $^{\cdot}O_2^-$ scavenging with different concentrations of CeO_2@ZIF-8.

UV-vis spectroscopy. As shown in Fig. 2F, UV-vis spectrum shows a special peak at 520 nm due to the reaction of salicylic acid (SA) with ˙OH generated by the Fenton reaction. As expected, CeO_2@ZIF-8 effectively scavenged the ˙OH free radical, as demonstrated by the decrease in absorbance at 520 nm and changes in color of the mixed solution. We also observed the strong antioxidant activity of the ligand 2-MI, while no free radical scavenging effect was observed for the Zn^{2+} ion (fig. S2, F and G), indicating that the antioxidant activity of ZIF-8 is attributed to the 2-MI ligand.

We then also conducted the EPR spectra to examine the $^{\cdot}O_2^-$ scavenging ability of CeO_2, ZIF-8, and CeO_2@ZIF-8. $^{\cdot}O_2^-$ was generated by the reaction of xanthine and xanthine oxidase and detected by the dihydroethidium (DHE) probe. As shown in Fig. 2G, all three NPs reduced the EPR amplitude of DMPO-OOH, especially the CeO_2@ZIF-8 composite nanomaterials. Furthermore, we also examined the $^{\cdot}O_2^-$ scavenging ability of CeO_2@ZIF-8 using DHE probe by fluorescence spectra. As shown in Fig. 2H, CeO_2@ZIF-8 decreased the intensity of the special peak in a dose-dependent manner, which was much higher than those of CeO_2 NPs and ZIF-8 alone. The formation of CeO_2@ZIF-8 notably decreased the surface area, pore volume, and pore size of ZIF-8 (fig. S3). Such a more conservative shell encapsulation could help prevent the direct catalytic reaction on exposed CeO_2 active sites, thus achieving better long-term and controllable effects.

Protection of pheochromocytoma cells by CeO_2@ZIF-8 against oxidative stress–induced damage

The rat adrenal medulla pheochromocytoma PC12 cell line has general characteristics of neuroendocrine cells, which is widely used in the study of neurophysiology and neuropharmacology. Therefore, we used PC12 cells damaged by ROS oxidation as a cell model for ischemic injury in stroke and further examined the protection of CeO_2@ZIF-8 to PC12 cells against tert-butyl hydroperoxide (t-BOOH)–induced oxidative damage. First, we detected the cytotoxic effects of CeO_2, ZIF-8, and CeO_2@ZIF-8 nanomaterials against PC12 cells after 48-hour incubation. As shown in fig. S4A, none of the three NPs

exhibited cytotoxicity to PC12 cells. As illustrated in Fig. 3A, 20 μM t-BOOH significantly inhibited PC12 cell proliferation and induced the cells' viability at 55.6%. CeO_2, ZIF-8, and CeO_2@ZIF-8 nanomaterials reversed cell damage induced by t-BOOH, especially CeO_2@ZIF-8. Furthermore, CeO_2@ZIF-8 protects PC12 cells from t-BOOH–induced oxidative damage in a dose-dependent manner (fig. S4B). Apoptosis is the main action mode of t-BOOH to cause cell growth inhibition. Therefore, we performed the annexin V and propidium iodide (PI) costaining assay to examine the reversal of t-BOOH–induced apoptosis by CeO_2@ZIF-8. As shown in Fig. 3B, t-BOOH notably enhanced PC12 cell apoptosis, especially in late stage, while CeO_2@ZIF-8 effectively reduced the cell apoptosis in a dose-dependent manner. For instance, 20 μM t-BOOH induced cell apoptosis at late stage with 57.2%, while after being cotreated with CeO_2@ZIF-8 (4 μg/ml), the cell apoptosis at late stage decreased to 9.1%. Then, we further used flow cytometry to examine the apoptotic cell death and cell cycle distribution of PC12 cells exposed to t-BOOH and CeO_2@ZIF-8. As shown in Fig. 3C and fig. S4C, CeO_2@ZIF-8 could reduce t-BOOH–induced PC12 cell apoptosis and cell cycle arrest. CeO_2@ZIF-8 protecting PC12 cells from t-BOOH–induced oxidative damage may be due to its efficient free radical scavenging ability. Excess intracellular ROS cause DNA damage and induce cell apoptosis. Therefore, we further tested the ability of CeO_2@ZIF-8 to scavenge intracellular ROS by DCFH-DA (2′-7′-dichlorodihydrofluorescein diacetate) assay. As shown in Fig. 3D, t-BOOH notably promoted ROS overproduction in PC12 cell to 140% in the first 18 min, and the ROS level remained at 120% even at 120 min. However, after incubation with CeO_2@ZIF-8, ROS generation in t-BOOH–treated PC12 cells was notably reduced. For instance, CeO_2@ZIF-8 (4 μg/ml) rapidly scavenged intracellular ROS generation to 105% in the first 18 min and further reduced the ROS level to the initial state of PC12 cells by 66 min. Furthermore, we also used fluorescence imaging to examine the fluorescence intensity of ROS levels in t-BOOH–damaged PC12 cells after treatment with CeO_2@ZIF-8. As shown in fig. S4D, t-BOOH triggered the ROS overproduction in PC12 cells, as reflected by the notable increase in green fluorescence. CeO_2@ZIF-8 notably reduced the fluorescence intensity in PC12 cells in a

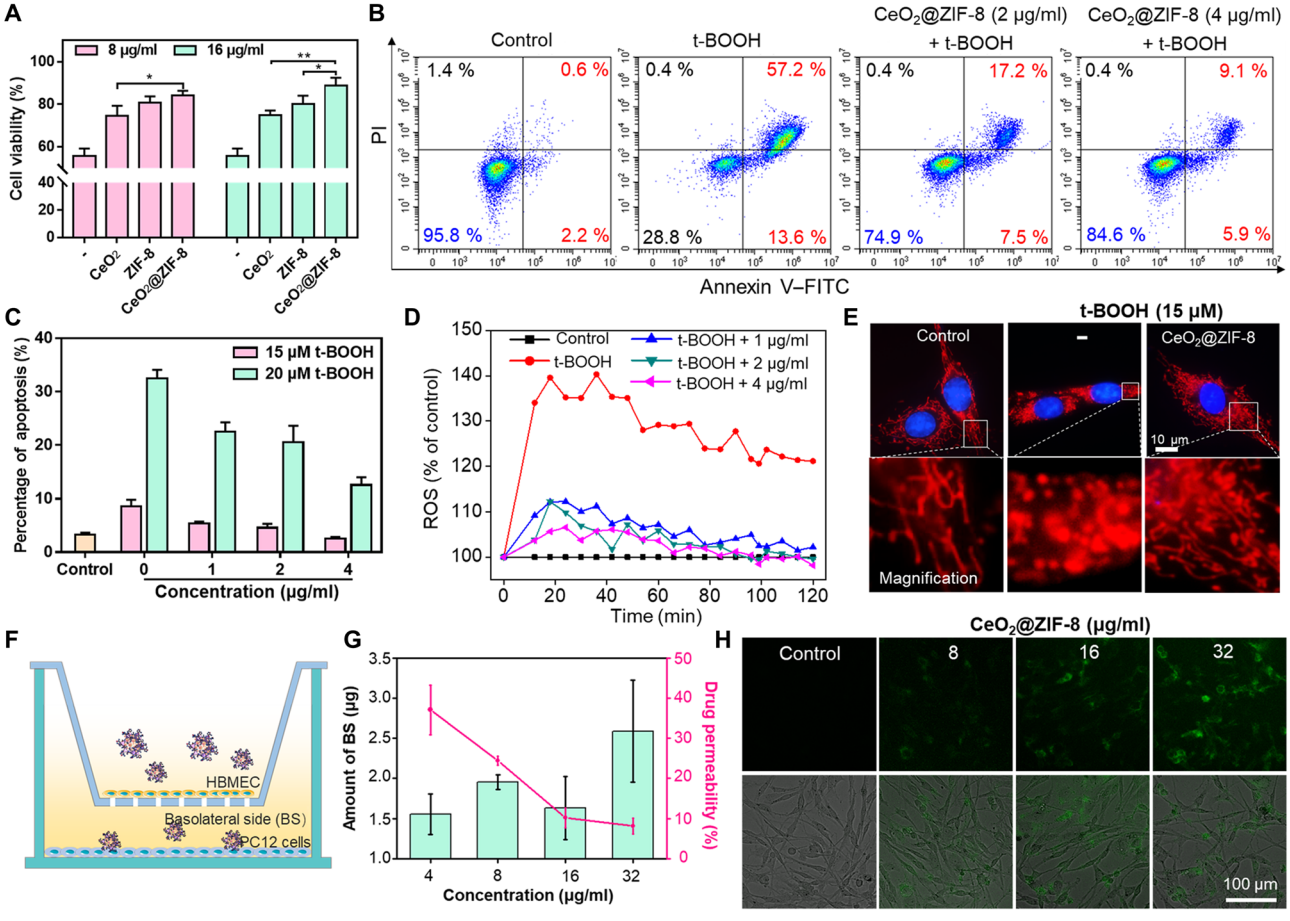

Fig. 3. Protection of CeO_2@ZIF-8 to PC12 cells against t-BOOH–induced oxidative damage. (**A**) The cell viability of PC12 cells cotreated with 20 μM t-BOOH and CeO_2, ZIF-8, or CeO_2@ZIF-8 nanomaterials for 48 hours. *$P < 0.05$ and **$P < 0.01$. (**B**) Annexin V–fluorescein isothiocyanate (FITC)/PI double staining to evaluate the reversal of t-BOOH–induced apoptosis by CeO_2@ZIF-8. PC12 cells were treated with t-BOOH and various concentrations of CeO_2@ZIF-8 for 48 hours. (**C**) CeO_2@ZIF-8 reduces t-BOOH–induced PC12 cell apoptosis. PC12 cells were treated with t-BOOH and various concentrations of CeO_2@ZIF-8 for 48 hours. (**D**) CeO_2@ZIF-8 blocks t-BOOH (15 μM)–induced ROS generation in PC12 cells. (**E**) CeO_2@ZIF-8 inhibits t-BOOH–induced mitochondrial fragmentation in PC12 cells. (**F**) Schematic demonstration of the transwell assay for the coculture of BBB model. (**G**) Penetrative capacity and ratio of CeO_2@ZIF-8 across BBB. (**H**) Internalization of the penetrative CeO_2@ZIF-8 in the lower chamber of PC12 cells after penetrating BBB for 24 hours.

dose-dependent manner, indicating the effective ROS scavenging in cell model by CeO_2@ZIF-8.

Mitochondria are major organelles for energy generation and the main source of generation of ROS, which play an important role in regulating the cell function and fate (*34*). If the excess superoxide is not cleared by intracellular antioxidants or related enzymes, it will lead to oxidative stress damage and dysfunction of mitochondria, resulting in cell death and other lesions. As illustrated in Fig. 3E, the mitochondria in healthy cells exhibit the filamentous mitochondrial network, while after incubation with 15 μM t-BOOH, the mitochondria were obviously destroyed severe fragments. Moreover, CeO_2@ZIF-8 effectively inhibited the mitochondrial fragmentation by t-BOOH. The morphological improvements further indicated that CeO_2@ZIF-8 could protect PC12 cells from t-BOOH–induced mitochondrial fragmentation through scavenging intracellular excess ROS.

Enhancement of transportation across the BBB of CeO_2@ZIF-8 and the endocytosis by PC12 cells

The capacity to penetrate across BBB is an essential factor for drug delivery to cure ischemic cerebral stroke. Although BBB can be disrupted by excess ROS during ischemia-reperfusion in stroke, studies also found that the damaged BBB in opening state lasts for only several hours (*35*, *36*). Therefore, the permeability of nanodrugs across the BBB to enhance its accumulation in the brain lesion is essential for stroke therapy. In this study, we conducted transwell assay for the coculture of human brain microvascular endothelial cell (HBMEC)/PC12 cell to simulate the BBB model and evaluated the permeability of coumarin 6 (C6)–labeled CeO_2@ZIF-8 (Fig. 3F). As shown in Fig. 3G, CeO_2@ZIF-8 effectively transports across the HBMECs after 24-hour incubation, and the transport ratios of CeO_2@ZIF-8 NPs at 4 μg/ml reached 37.1%. In addition, we also examined the internalization of the penetrative CeO_2@ZIF-8 in the lower chamber of PC12 cells by fluorescence imaging. As shown in Fig. 3H, the fluorescence intensities of C6-labeled CeO_2@ZIF-8 in PC12 cells were enhanced in a dose-dependent manner, which suggested the high permeability of CeO_2@ZIF-8 through the BBB.

Lysosome-mediated endocytosis is an important mechanism for nanomaterials to enter cells (*37*). In this study, we examined the localization of CeO_2@ZIF-8 in PC12 cells by TEM and fluorescence imaging and proposed a cell internalization mechanism (Fig. 4A). As shown in Fig. 4B and fig. S5A, CeO_2 nanopolyhedra, but not CeO_2@ZIF-8, were found in the lysosome of the cell. This may be due to the degradation of the outer framework of ZIF-8 in the lysosomal environment. Therefore, we further examined the morphological changes of CeO_2@ZIF-8 after incubation in different pH of PBS solutions for 12 hours by TEM. As shown in Fig. 4C, after being shaken for 12 hours in PBS at pH 7.4 (simulating the physiological condition), CeO_2@ZIF-8 still maintained the same morphology as that in aqueous solution. After incubation in PBS at pH 5.3 with lysozyme (simulating the acidic lysosomal environment), the outer framework of ZIF-8 was cracked, leaving CeO_2 nanopolyhedra, indicating that the ZIF-8 NPs can be degraded in the lysosomal environment. To further explore this hypothesis, we then synthesized the C6-labeled CeO_2@ZIF-8 to explore its intracellular trafficking by fluorescence imaging. First, PC12 cells were stained with special fluorescent tracers, LysoTracker (red) and Hoechst 33342 (blue). Figure 4D shows that C6-labeled CeO_2@ZIF-8 (green fluorescence) gathered in the cell membrane after 0.5-hour treatment and started to enter in lysosomes at 1 hour. Furthermore, the green fluorescence of C6-labeled CeO_2@ZIF-8 matches well with the red fluorescence from LysoTracker after 2-hour incubation, and the green fluorescence intensity enhanced gradually thereafter. These images suggest that CeO_2@ZIF-8 internalizes in PC12 cells through lysosome-mediated endocytosis.

To further explore the internalization pathway of CeO_2@ZIF-8 in PC12 cells, we examined the cellular uptake behavior after being performed with different chemical endocytosis inhibitors. First, we examined the quantitative cellular uptake of CeO_2@ZIF-8 in PC12 cells, finding that the intracellular concentration of nanomaterials increased in a time- and dose-dependent manner in PC12 cells (Fig. 4E). We then explored the cellular uptake of CeO_2@ZIF-8 in PC12 cells after pretreatment with different endocytosis inhibitors. As shown in Fig. 4F, these endocytosis inhibitors significantly inhibit the internalization of CeO_2@ZIF-8 in PC12 cells, especially the nystatin, suggesting that lipid raft–dependent endocytosis was the main pathway. Furthermore, sodium azide (NaN_3), chlorpromazine (CPZ), and low temperature (4°C) are the inhibitors of energy-dependent endocytosis. From the results, we found that these effectively inhibited the cellular uptake of CeO_2@ZIF-8, especially the combined treatment of NaN_3 and CPZ with low temperature, respectively. Sucrose is a specific inhibitor of clathrin-mediated endocytosis, and dynasore acts as an inhibitor of dynamin-mediated lipid raft endocytosis. After cotreatment with 4°C, these two inhibitors further decreased the internalization of CeO_2@ZIF-8 in PC12 cells (Fig. 4G). Together, both energy- and lipid raft–dependent endocytosis were the main pathways of CeO_2@ZIF-8 being internalized in PC12 cells.

In vivo antagonism of ischemic stroke by CeO_2@ZIF-8

To further confirm the in vivo brain protection of CeO_2@ZIF-8, we established the MCAO rat model to simulate the generating process of ischemia-reperfusion in stroke. The MCAO model was formed by inserting the filament with a silicone tip into the middle cerebral artery of the rat for 90 min, and then the filament was removed to form the reperfusion. The infarct areas and neurological scores of MCAO mice were analyzed after treatment with CeO_2@ZIF-8 for 3 days. As shown in Fig. 5 (A and B), the MCAO model mice with saline injection only showed large-area infarction, which is reflected by the inability stained by 2,3,5-triphenyltetrazolium chloride (TTC), while after treatment with CeO_2@ZIF-8 for 3 days in MCAO mice, the brain infarct area significantly decreased in a dose-dependent manner. For instance, a large infarct area with ~42.3% was detected in the saline group, while after injection with CeO_2@ZIF-8 at 0.2 and 0.4 mg/kg, the infarct area decreased to 23.1 and 15.7%, respectively. Furthermore, the neurological scores of MCAO mice after treatment with CeO_2@ZIF-8 also improved (Fig. 5C). The body weight of MCAO mice showed little change in each treatment group (fig. S5B), indicating the high in vivo anti–ischemic stroke activity and low toxicity of CeO_2@ZIF-8 nanosystem. To further explore the enhancement of brain protection of CeO_2@ZIF-8, we also constructed C57 mice MCAO model to examine the effects of different nanomaterials on the infarct areas and neurological scores after treatment for 3 days. As shown in fig. S6 (A and B), CeO_2 NPs, ZIF-8, and CeO_2@ZIF-8 significantly decreased the brain infarct area, especially CeO_2@ZIF-8. We also conducted the Bederson's scoring system and elevated body swing test to evaluate the effects of these NPs on the function and behavior of the MCAO mice. The results showed that treatments with CeO_2, ZIF-8, and CeO_2@ZIF-8 effectively improved the function and behavior of MCAO mice, with better effects found in the CeO_2@ZIF-8 group (fig. S6, C to E).

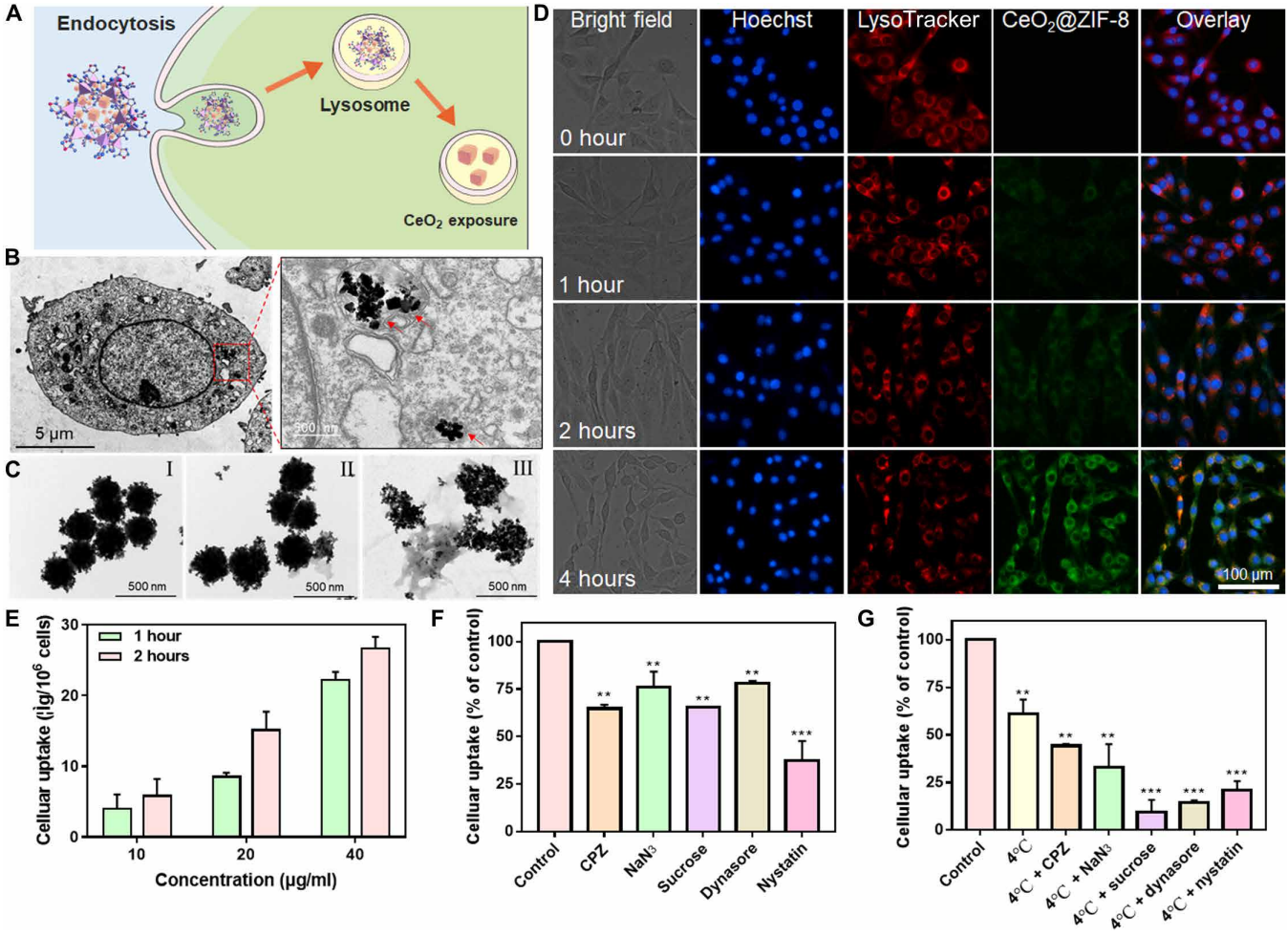

Fig. 4. Endocytosis of CeO_2@ZIF-8 in PC12 cells. (**A**) Schematic demonstration of endocytosis of CeO_2@ZIF-8 in PC12 cells. (**B**) TEM image of CeO_2@ZIF-8 internalized in PC12 cells. PC12 cells were incubated with CeO_2@ZIF-8 (16 μg/ml) for 6 hours. (**C**) TEM images of CeO_2@ZIF-8 in aqueous (I), PBS (pH 7.4; II), and PBS (pH 5.3 with lysozyme; III) after shaking for 12 hours. (**D**) Intracellular trafficking of C6-labeled CeO_2@ZIF-8 (20 μg/ml; green fluorescence) in PC12 cells. The cells were stained with special fluorescent tracers: LysoTracker (red) and Hoechst 33342 (blue). (**E**) Quantitative analysis of cellular uptake of CeO_2@ZIF-8 in PC12 cells by determination of fluorescence intensity. (**F** and **G**) Intracellular uptake inhibition by different endocytosis inhibitors. The cells were pretreated with different endocytosis inhibitors for 1 hour and then incubated with CeO_2@ZIF-8 (10 μg/ml) for 2 hours at 37° or 4°C. The control group was incubated with CeO_2@ZIF-8 at 37°C only. $^{**}P < 0.01$ and $^{***}P < 0.001$.

To further investigate the mechanism of the anti–ischemic stroke activity, we first examined the internalization of CeO_2@ZIF-8 in the brain tissue of MCAO mice using in vivo fluorescence imaging and TEM observation. As shown in fig. S7A, indocyanine green (ICG)–labeled CeO_2@ZIF-8 can quickly accumulate into brain tissue after intravenous injection, indicating that this nanosystem can cross BBB along with the restored perfusion in MCAO mice. Furthermore, from the TEM image of brain tissue, CeO_2 nanopolyhedra were found in the brain tissue of MCAO mice after intravenous injection three times with CeO_2@ZIF-8 for 3 days (Fig. 5D and fig. S7B). The results indicated that CeO_2@ZIF-8 can penetrate BBB to reach brain tissue and break down the outer ZIF-8 to release a large amount of CeO_2 nanopolyhedra. Therefore, we then further examined the biodistribution of Ce in the main organs of mice after intravenous injection with CeO_2 and CeO_2@ZIF-8. As shown in Fig. 5E, compared with the treatment group of CeO_2, the content of Ce in brain tissue was significantly enhanced and decreased in the liver tissue after injection with CeO_2@ZIF-8, suggesting that CeO_2@ZIF-8 composite nanomaterials decrease the clearance of the free CeO_2 by murine macrophages in liver and thus enhance their accumulation in brain tissues. Further studies were conducted to explore the metabolism of CeO_2@ZIF-8 in the main organs for a long time. As shown in fig. S7C, we found that the accumulation of Ce in liver, spleen, and kidney significantly decreased after intravenous injection with CeO_2@ZIF-8 for 7 and 14 days, indicating that CeO_2@ZIF-8 can effectively be cleared out in vivo. To further verify this hypothesis, we then investigated the pharmacokinetic property of CeO_2 and CeO_2@ZIF-8 in SD mice. First, the concentration of Ce in plasma after injection of CeO_2@ZIF-8 was much higher than that of the free CeO_2 group (Fig. 5F). Furthermore, from the related pharmacokinetic parameters of these two nanomaterials, the elimination rate (k10, k12, and k21) and clearance of CeO_2@ZIF-8 significantly decreased compared with the free CeO_2 nanopolyhedra after loading into the framework of ZIF-8 (table S1). The half-life ($t_{1/2}$ alpha and $t_{1/2}$ beta) and mean retention time of CeO_2@ZIF-8 were much higher than those of the free CeO_2 nanopolyhedra. These results showed that

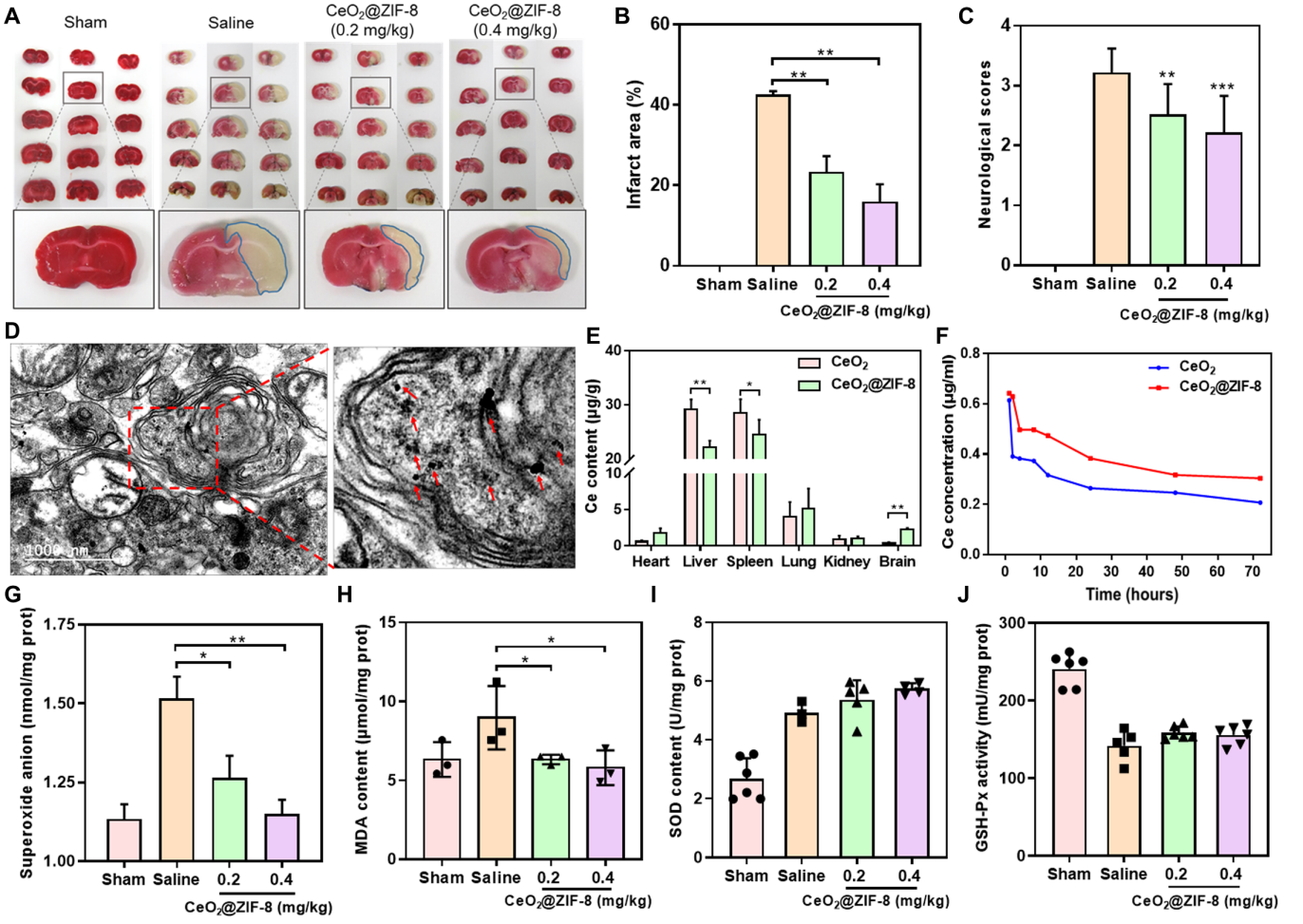

Fig. 5. CeO_2@ZIF-8 reduces infarct volume by reducing ROS-induced oxidative damage. (**A**) Representative images of TTC-stained brain slices after treatment with CeO_2@ZIF-8 for 3 days in MCAO mice model ($n = 4$). (**B**) Corresponding infarct areas of different groups analyzed by ImageJ ($n = 4$). (**C**) Neurological scores of MCAO mice after treatment with CeO_2@ZIF-8 for 3 days ($n = 10$). (**D**) Assessment of CeO_2@ZIF-8 (0.4 mg/kg) internalization in the brain tissue of MCAO mice for 3 days using TEM imaging ($n = 3$). (**E**) Biodistribution of Ce in the mice main organs after intravenous injection with CeO_2 and CeO_2@ZIF-8 ($n = 5$) for 3 days. (**F**) Ce content in plasma versus time after intravenous injection with CeO_2 and CeO_2@ZIF-8 ($n = 5$). (**G** to **J**) Expression levels of superoxide anion (G), MDA (H), SOD (I), and GSH-Px (J) in the brain tissue of different treatment groups ($n = 3$). Significant difference between treatment and control groups is indicated at $^*P < 0.05$, $^{**}P < 0.01$, and $^{***}P < 0.001$ levels.

loading CeO_2 into ZIF-8 could effectively prolong the blood circulation time of CeO_2, reduce the clearance rate, and enhance the accumulation in brain tissue.

On the basis of the efficient ROS scavenging ability of CeO_2@ZIF-8 in vitro, we then further explored the mechanism of the anti–ischemic stroke activity through scavenging the ROS in vivo. As shown in Fig. 5G, the superoxide anion in the brain tissue of the MCAO model mice with saline injection only was significantly increased compared with the sham-operated control group. However, after injection with CeO_2@ZIF-8 for 3 days in MCAO mice, the superoxide anion level decreased in a dose-dependent manner. Malondialdehyde (MDA) is one of the most important products of membrane lipid peroxidation, which affects the activities of respiratory chain complexes and key enzymes in mitochondria. Therefore, we also examined the production of MDA in the brain tissue of the MCAO mice and found that the MDA level in the brain tissue of the MCAO mice after treatment with CeO_2@ZIF-8 was much lower than that in the MCAO mice with saline injection only (Fig. 5H). Superoxide dismutase (SOD) and glutathione peroxidase (GSH-Px) are both important antioxidative enzymes in the human body, which exhibit efficient ROS scavenging ability to repair cells and reduce the damage by ROS. In this study, we then further examined the SOD and GSH-Px contents in brain tissues of MCAO mice. As shown in Fig. 5I, the SOD content in brain tissue of the MCAO mice was much higher than that in the sham-operated control group, indicating that oxidative stress causes the up-regulation of SOD, while after injection with CeO_2@ZIF-8 at 0.2 and 0.4 mg/kg three times, the SOD content in the brain tissue of these treated MCAO mice did not increase further. Even in the brain tissue of these MCAO mice, the GSH-Px content was decreased compared with control group (Fig. 5J). These results indicate that CeO_2@ZIF-8 inhibits lipid peroxidation in brain tissues of MCAO mice by direct scavenge of ROS overproduction, but not up-regulation of enzymatic activities of SOD and GSH-Px.

Furthermore, we also elucidated the therapeutic effects of CeO_2@ZIF-8 as a neuroprotective agent by pathological analysis in brain tissue. First, from the results of hematoxylin and eosin (H&E) staining in brain sections of MCAO mice, the group of saline injection only showed massive necrosis in the cerebral infarction area, while

CeO_2@ZIF-8 notably decreased the area of necrosis (Fig. 6A). Therefore, we also examined the damage to neurons in the infarcted area of MCAO mice using Nissl staining. As shown in Fig. 6B, compared with the sham-operated control group, the number of intact neurons was notably decreased and exhibited irregular morphology and disordered arrangement in the infarcted area of MCAO mice with saline injection only. However, after treatment with CeO_2@ZIF-8 for 3 days in MCAO mice, the neuron damage in brain tissue decreased in a dose-dependent manner. In addition, from the result of TUNEL (terminal deoxynucleotidyl transferase–mediated deoxyuridine triphosphate nick end labeling)–Hoechst costaining assay in brain sections of MCAO mice, the group of saline injection exhibited typical apoptotic characteristics in the infarcted area, while CeO_2@ZIF-8 notably decreased the apoptosis of neurons in a dose-dependent manner (Fig. 6C). These results further indicate that CeO_2@ZIF-8 effectively inhibits the damage and apoptosis of neurons, thus reducing the further oxidative damage caused by ischemia-reperfusion in stroke.

CeO_2@ZIF-8 suppresses inflammation and immune response induced by reperfusion in ischemic stroke

A large number of glial cells proliferate and activate during ischemia-reperfusion injury, resulting in strong inflammatory reaction and glial scar formation, ultimately causing the further injury by inflammation (*28*, *33*). Among them, astrocytes and microglia are the main inflammatory cells in brain tissue, and their activation reflects the state of inflammation in the brain. Therefore, we have examined the expression level of glial fibrillary acidic protein (GFAP; a marker of astrocytes) and ionized calcium–binding adaptor molecule-1 (Iba-1; a marker of microglia) in brain sections of MCAO mice by immunohistochemical staining. As shown in Fig. 6D, compared with the sham-operated control group, the expression levels of GFAP and Iba-1 were much higher in brain sections of MCAO mice with saline injection only, indicating that MCAO model induces enhancement in the number of astrocytes and microglia. After treatment with CeO_2@ZIF-8 for 3 days in MCAO mice, the number of GFAP- and Iba-1–positive cells was significantly decreased in a dose-dependent manner (Fig. 6, E and F). We also examined the proinflammatory cytokines of tumor necrosis factor–α (TNF-α) and various kinds of interleukins, such as IL-1β and IL-6 secreted in the infarct part of the brain tissue of the MCAO mice. As shown in Fig. 6 (G to I), MCAO model induced significant enhancement secretion of TNF-α, IL-1β, and IL-6 in brain tissue compared with the sham-operated control group. After treatment with CeO_2@ZIF-8 for 3 days in MCAO mice, the levels of these proinflammatory cytokines showed

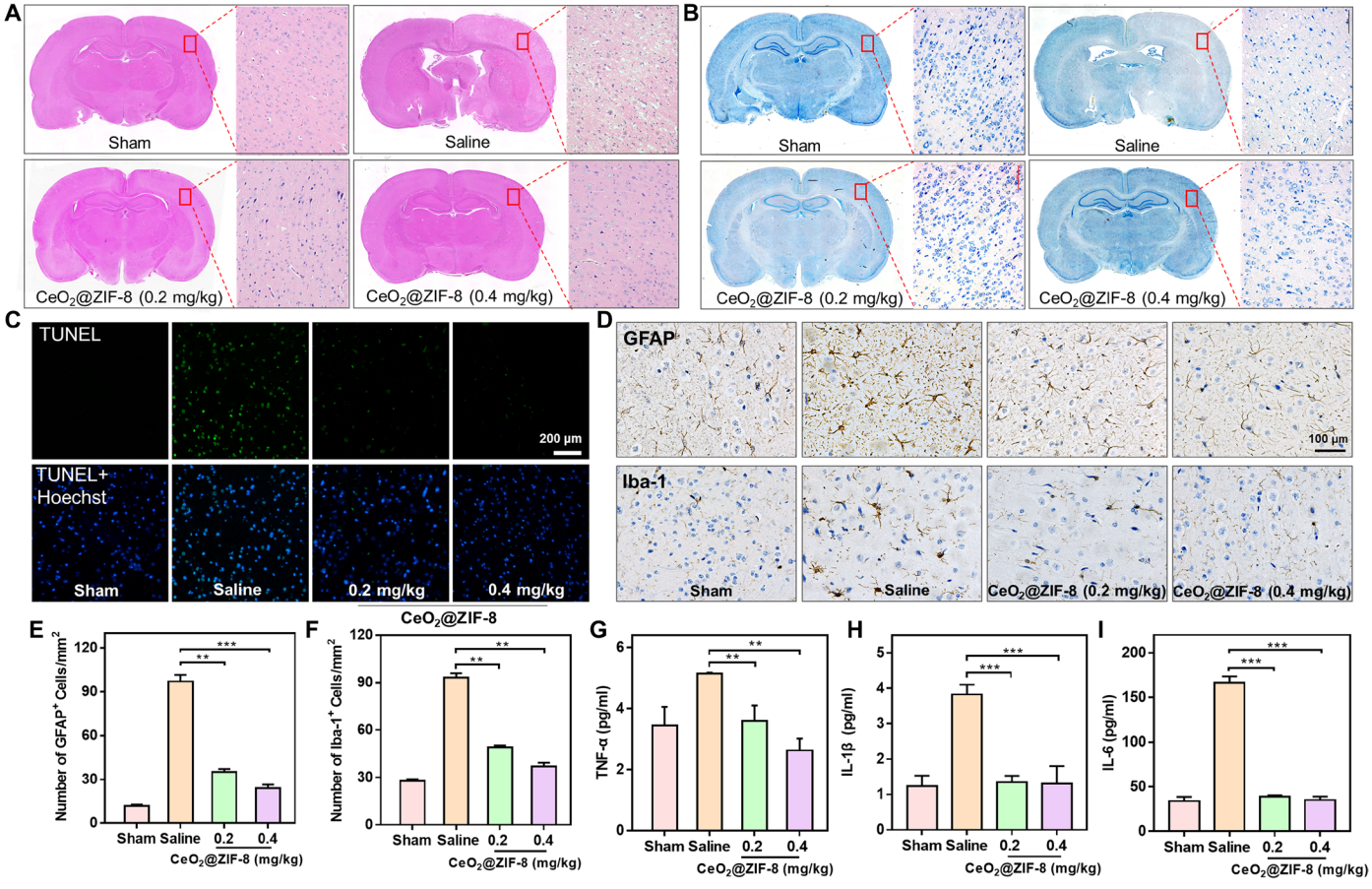

Fig. 6. Therapeutic effects of CeO_2@ZIF-8 and its suppression on inflammation and immune response induced by reperfusion in ischemic stroke. Representative photomicrographs of H&E staining (**A**), Nissl staining (**B**), and TUNEL (terminal deoxynucleotidyl transferase–mediated deoxyuridine triphosphate nick end labeling)–Hoechst costaining (**C**) of brain tissues from different treatment groups. (**D**) GFAP and Iba-1 expression in brain sections of MCAO mice from different treatment groups examined by immunohistochemical staining ($n = 3$). (**E** and **F**) The number of $GFAP^+$ cells (E) and Iba-1^+ cells (F) in brain sections of MCAO mice from different treatment groups. (**G** to **I**) Inflammatory factors of TNF-α (G), IL-1β (H), and IL-6 (I) in different treatment groups ($n = 3$) in the infarct part of the brain tissue. $^{**}P < 0.01$ and $^{***}P < 0.001$.

different degree drops in a dose-dependent manner. These results suggest that CeO_2@ZIF-8 could effectively inhibit the activation of the astrocytes and microglia during ischemia-reperfusion injury, thus reducing further injury by inflammation.

Toxic side effects of nanomedicine on human body are an important limitation for their future biomedical application. Therefore, we further performed the histological analysis in the main organs by H&E staining in these MCAO mice. As shown in fig. S8, the sections of major organs, including heart, liver, spleen, lung, and kidney, did not exhibit the obvious inflammation or other pathological changes after treatment with CeO_2@ZIF-8 for 3 days in MCAO mice. Furthermore, we also examined the in vivo toxicity of CeO_2@ZIF-8 in healthy mice for a long time. The hematological and pathological analysis reveals that, after 14-day treatment, CeO_2@ZIF-8 demonstrated no obvious damage to these major organs of the mice under this experimental condition (fig. S9), indicating the safety potency of this nanosystem in future application. Together, this study demonstrates an effective and safe ROS scavenging agent to protect the ischemia-reperfusion injury during stroke in vivo.

Currently, for clinical use purposes, it is urgently needed to design and develop agents with potent antioxidative activities and desirable physicochemical property for the treatment of ischemia strokes. Therefore, in this study, we have rationally designed and synthesized ZIF-capped CeO_2 NPs (CeO_2@ZIF-8 NPs) with enhanced catalytic and antioxidative activities. This smart design could overcome the drawbacks of CeO_2 NPs and achieve the following advantages: (i) The surface ZIF-8 acts as peroxidase to maintain the antioxidant activity in the presence of excessive H_2O_2 or other oxidants, which can absorb H_2O_2 and destroy the O—O bond to disintegrate H_2O_2. (ii) The ZIF-8 frame growing on the outer layer of CeO_2 NPs controls the size, shape, and surface charge of CeO_2 core to make it more suitable for biological application. (iii) The decomposition of ZIF-8 results in release of active components, synergistically enhancing the stroke therapeutic efficacy of CeO_2. (iv) CeO_2@ZIF-8 also suppresses the inflammation- and immune response–induced injury by suppressing the activation of astrocytes and secretion of proinflammatory cytokines, thus achieving satisfactory prevention and treatment in neuroprotective therapy during ischemic stroke with high safety. As expected, this nanosystem effectively inhibits the lipid peroxidation in brain tissues of MCAO model mice, reducing the oxidative damage and apoptosis of neurons in brain tissue. Together, this study not only provides a new in situ synthetic approach of synergistic nanotherapeutics by using ZIF as bioactive surface decoration and CeO_2 NPs as functional core but also sheds light on the neuroprotective application mechanisms against reperfusion-induced injury in ischemic stroke.

MATERIALS AND METHODS

Materials

$Zn(NO_3)_2{\cdot}6H_2O$, 2-methylimidazole, and SA were purchased from Macklin Company (Shanghai, China). $Ce(NO_3)_2{\cdot}6H_2O$ and polyvinylpyrrolidone (PVP) were purchased from Aladdin Company (Shanghai, China). DMEM and FBS were purchased from Gibco. Thiazolyl blue tetrazolium bromide (MTT) and DHE were purchased from Sigma-Aldrich. TTC was purchased from Sangon Biotech (Shanghai) Co. Ltd. 5,5-Dimethyl-1-pyrroline *N*-oxide was purchased from Dojindo Company. All enzyme-linked immunosorbent assay (ELISA) kits were purchased from Thermo Fisher Scientific.

Synthesis and characterization of CeO_2@ZIF-8

First, to obtain CeO_2 nanopolyhedra, 0.05 M $Ce(NO_3)_2{\cdot}6H_2O$ and 0.01 M NaOH were dissolved in 40-ml deionized water and magnetically stirred until fully dissolved. Then, the mixture solution was removed to a Teflon bottle and held in a stainless steel vessel autoclave. The autoclave was transferred into thermal treatment for 24 hours at 180°C. The products were washed by deionized water three times at 12,000 rpm, and the CeO_2 nanopolyhedra were obtained. Successively, 3.5 mg of CeO_2 nanopolyhedra and 100 mg of PVP were dissolved with 5-ml methanol solution, stirred at room temperature for 24 hours, collected by centrifugation, and stored in 100 μl of methanol to obtain PVP-CeO_2. Then, 3.5 mg of PVP-CeO_2 was added into 5 ml of 2-methylimidazole (25.6 mM, dissolved in methanol solution) and stirred for 15 min, and then 5 ml of 25.2 mM $Zn(NO_3)_2{\cdot}6H_2O$ methanol solution was added in this mixed solution and stirred for another 20 min at room temperature. The products were centrifuged at 12,000 rpm for 10 min and washed with methanol three times. Last, the CeO_2@ZIF-8 nanomaterials were obtained by vacuum drying.

The as-synthesized CeO_2 nanopolyhedra, ZIF-8, and CeO_2@ZIF-8 nanomaterials were characterized by different microscopic and spectroscopic analyses. Briefly, TEM (Hitachi H-7650, 100 kV), scanning electron microscope (Zeiss EVO 18, 20 kV), and high-resolution TEM (JEOL 2010) were used to characterize their morphology. Meanwhile, the size distribution and zeta potential were detected by Zetasizer Nano ZS. The Fourier transform infrared spectroscopy (Equinox 55, Bruker), UV-vis–NIR (near-infrared) spectrophotometry (UH-4150 Spectrophotometer, Hitachi), and Raman spectra (LabRAM HR Evolution, HORIBA) were used to determine the chemical composition of these nanomaterials. XRD pattern and XPS spectra were conducted using MSAL XD-2 x-ray diffractometer and Thermo ESCALAB 250Xi, respectively. Scavenging free radical ability was detected by EPR (A300, Bruker) and fluorescence spectrum (Lumina Fluorescence, Thermo Fisher Scientific).

ABTS free radical scavenging assay

ABTS scavenging assay was used to evaluate the antioxidant activity of CeO_2, ZIF-8, and CeO_2@ZIF-8. Briefly, the ABTS free radical ($ABTS^{\bullet+}$) was formed by ABTS stock solution (5 mM, dissolved in PBS) reacted with manganese bioxide solution according to the previously described method (*38*). The different concentrations of CeO_2, ZIF-8, and CeO_2@ZIF-8 were mixed with $ABTS^{\bullet+}$ radical solution, and then the absorbance at 734 nm within 60 min was examined using a cell imaging multi-mode reader (Cytation 5, BioTek Instruments Inc.).

Scavenge H_2O_2 by in situ Raman spectra

CeO_2, ZIF-8, and CeO_2@ZIF-8 nanomaterials (10 mg) were dried in desiccator at room temperature for 12 hours and transferred to a clean glass sheet, where 50 μl of 10% H_2O_2 was added in the surface. Under the excitation of 488-nm laser, the samples were measured with a laser Raman microscope in the time range of 0, 20, and 40 min. H_2O_2 was then dropped into the same location of the sample immediately.

Scavenge $^{\bullet}OH$ and $^{\bullet}O_2^-$ by EPR spectra analysis and fluorescence spectrum

First, $^{\bullet}OH$ was generated through Fenton reaction with Fe^{2+}/H_2O_2 system by 1.8 mM $FeSO_4$ and 5 mM H_2O_2 for 10 min. In addition,

$^{\bullet}O_2^-$ was generated from the production of xanthine (0.5 mM) and xanthine oxidase (0.1 U/ml) at room temperature for 30 min. Then, the $^{\bullet}OH$ and $^{\bullet}O_2^-$ scavenging abilities of CeO_2, ZIF-8, and CeO_2@ZIF-8 were examined by EPR spectra analysis: CeO_2, ZIF-8, and CeO_2@ZIF-8 (15 μg/ml) were added into the obtained $^{\bullet}OH$ or $^{\bullet}O_2^-$ radical solution and incubated for another 30 min. After that, DMPO was added to the mixture solution for 10 min using EPR to detect the ability of three NPs to scavenge $^{\bullet}OH$ and $^{\bullet}O_2^-$ radical. The $^{\bullet}OH$ scavenging ability of CeO_2, ZIF-8, and CeO_2@ZIF-8 indirectly detected the products of 2,3-dihydroxybenzoic acid by UV-vis spectra, which generated SA (2 mM) and $^{\bullet}OH$ radical, and exhibited the characteristic absorbance at 510 nm. The $^{\bullet}O_2^-$ scavenging ability of CeO_2, ZIF-8, and CeO_2@ZIF-8 was examined by using DHE fluorescence probe.

Cell culture, cell line, and cytotoxicity evaluation

PC12 and HBMEC lines were purchased from the American Type Culture Collection. PC12 cells and HMBECs were incubated in DMEM and RPMI 1640 with FBS (10%), respectively, and penicillin (100 U/ml) and streptomycin (50 U/ml) were added at 37°C in a 5% CO_2 incubator. MTT assay was used to detect the cytotoxicity and reverse damage of CeO_2@ZIF-8 to PC12 cells induced by t-BOOH. Briefly, PC12 cells (4×10^3 per well) were seeded in 96-well plates. After cell adherence, various concentrations of t-BOOH and drugs were successively added to each well and incubated for another 48 hours, and cell viability was determined by MTT assay (*39*).

Real-time living cell imaging

Real-time localization of CeO_2@ZIF-8 in PC12 cells was observed by living cell imaging based on the fluorescence intensity of C6 loaded in CeO_2@ZIF-8. Briefly, PC12 cells (6×10^4 cells/ml, 2 ml) were seeded in 2-cm culture dishes and attached for 24 hours. The PC12 cells were stained with Hoechst 33342 (blue) and LysoTracker (red), and then C6-CeO_2@ZIF-8 (20 μg/ml; green) was added in the cells and captured by fluorescence microscopy at specific times.

Intracellular uptake of CeO_2@ZIF-8

For preparation of the C6-labeled CeO_2@ZIF-8, C6 was added in the PVP-CeO_2 reaction system before adding $Zn(NO_3)_2{\cdot}6H_2O$ with full stirring. The next step was similar to the preparation with CeO_2@ZIF-8. The cellular uptake of CeO_2@ZIF-8 in PC12 cells was measured on the basis of the fluorescence intensity of C6 loaded in CeO_2@ZIF-8 with a fluorescence microplate reader. Briefly, PC12 cells were seeded into 96-well plates with a density of 6×10^4 cells/ml. After cell adherence, the cells were incubated with different concentrations of C6-CeO_2@ZIF-8 for 1 and 2 hours, respectively. After removal of medium, the cells were rinsed with cold PBS three times to remove the particles outside the cells, and then 1% Triton X-100 solution was added to lysate the cells. Last, the fluorescence intensity of the treated cells was detected with a multi-mode cell imaging reader (Cytation 5, BioTek Instruments Inc.) at excitation and emission wavelengths of C6 (430 and 485 nm). The cellular uptake of C6-CeO_2@ZIF-8 in PC12 cells was calculated from the standard curve and expressed as the quantity (μg) per 10^6 cells. The cellular uptake behavior of CeO_2@ZIF-8 in PC12 cells was further investigated with different chemical endocytosis inhibitors, including NaN_3 (10 mM), CPZ (10 μg/ml), sucrose (0.45 M), dynasore (1.6 mM), and nystatin (10 μg/ml), and by pretreating cells at 37° or 4°C for 1 hour, and then the cellular uptake was examined according to the above method.

Mitochondrial fragmentation analysis

The mitochondrial fragmentation of PC12 cells induced by t-BOOH was determined by fluorescence imaging. Briefly, PC12 cells (6×10^4 cells/ml, 2 ml) were seeded in 35-mm confocal dishes with coverglass bottom and attached for 24 hours. The cells were stained with Hoechst 33342 (blue) and MitoTracker (red), and then 15 μM t-BOOH was added in the cells and incubated for 2 hours. The t-BOOH damaged cells were further incubated with or without CeO_2@ZIF-8 at 4 μg/ml for another 24 hours. After rinsing three times with cold PBS, the cells were examined on mitochondrial morphology under a fluorescence microscope (EVOS FL, 100× objective lens).

Evaluation of intracellular ROS

Briefly, PC12 cells (2×10^5 cells/ml) were seeded in 96-well plates. After cell adherence, the PC12 cells were prestained with DCFH-DA for 30 min. Next, the cells were incubated with t-BOOH (15 μM) and different concentrations of CeO_2@ZIF-8 for 2 hours; meanwhile, the blank control group did not add drugs, and other experiments were the same as the experimental group. The cells were analyzed for ROS generation within 120 min using a cell imaging multimode reader at excitation and emission wavelengths of 488 and 528 nm, respectively.

Cell cycle and apoptosis analysis

The flow cytometric analysis was used to determine the cell cycle and apoptosis of PC12 cells induced by t-BOOH and recovered ability of CeO_2@ZIF-8. Briefly, PC12 cells were treated with 15 or 20 μM t-BOOH for 2 hours, and then the different concentrations of CeO_2@ZIF-8 were added for another 48 hours. Then, the treated cells were collected and fixed with 75% ethanol solution and stained with PI in the dark. The stained cells were analyzed on a Beckman CytoFLEX S flow cytometer.

For analysis of cell apoptosis, PC12 cells were plated in 100-mm dishes with a density of 4×10^4 cells/ml. After cell adherence, the cells were treated with t-BOOH (20 μM) and various concentrations of CeO_2@ZIF-8 for 48 hours at 37°C. Then, after removing from the medium and washing with cold PBS, the cells were stained with annexin V and PI according to the experimental method in the assay kit (Solarbio) specification. Cell apoptosis was analyzed using a Beckman CytoFLEX S flow cytometer.

BBB assessment in vitro

In a previous study, HBMECs were used to establish the BBB model. Briefly, HBMECs were seeded in the upper chambers (3 μm, Corning, USA) with 1.5×10^5 cells and incubated for several days until the transendothelial electrical resistance reaches 330 ohm·cm^2. Then, the PC12 cells were then cultured in the lower chambers with a density of 8000 cells per well. After cell adherence, different concentrations of C6-CeO_2@ZIF-8 were added in the upper chambers for 24-hour incubation. After that, a fluorescence microscope was used to observe the internalization of C6-CeO_2@ZIF-8 in PC12 cells. Successively, the fluorescence intensity of C6-CeO_2@ZIF-8 in the lower chambers was detected with a Cytation 5 reader (BioTek Instruments Inc.). The amount of C6-CeO_2@ZIF-8 across BBB was calculated on the basis of standard curve.

Internalization of CeO_2@ZIF-8 in PC12 cells by TEM

PC12 cells (1.5×10^5 cells/ml) were seeded in 10-cm dishes. After cell adherence, the cells were incubated with CeO_2@ZIF-8 (16 μg/ml)

for 6 hours at 37°C. After rinse with cold PBS and collection using trypsin digestion, the cells were fixed in 4% glutaraldehyde diluted in PBS over 24 hours and subsequently embedded in gelatin (2% gelatin in PBS). The cell mass was the size of a mung bean, wrapped with 1% agarose, and rinsed with 0.1 M PBS three times (each time 15 min). Then, 1% osmic acid–0.1 M PBS was fixed at room temperature (20°C) for 2 hours. The samples were dehydrated with 50, 70, 80, 90, 95, and 100% alcohol and 100% acetone in turn. Epoxy resin was used to bury samples, which were then kept in electric oven at 37°C overnight. Then, the epoxy resin was polymerized by changing the electric oven temperature to 60°C for 48 hours. The ultrathin sections (60 to 80 nm) were obtained with an ultrathin slicer, dyed in 2% uranyl acetate–saturated alcohol solution and lead citrate for 15 min, and then dried overnight at room temperature. Last, the sample was observed under TEM.

In vivo protection against ischemic stroke

The MCAO mice model was established to evaluate the protection of CeO_2@ZIF-8 against ischemic stroke in vivo. Briefly, the MCAO model mice was formed by inserting the filament with silicone tip into the middle cerebral artery of the SD mice (250 to 300 g) for 90 min, and then the filament was removed to form the reperfusion. The sham-operated control group (10 mice) was established, consistent with the treatment of MCAO model except for the embolization. The MCAO model mice were randomly divided into three groups: saline group, CeO_2@ZIF-8 group (0.2 mg/kg), and CeO_2@ZIF-8 group (0.4 mg/kg) (10 mice per group). CeO_2@ZIF-8 was dispersed in saline solution and immediately injected at the caudal vein after reperfusion and injected every other day for 3 days. Neurological scores of MCAO mice after treatment with CeO_2@ZIF-8 were determined using a modified Bederson's scoring system within 3 days. Elevated body swing test was also used to evaluate the function and behavior of MCAO mice exposed to CeO_2, ZIF-8, and CeO_2@ZIF-8. The number of swings to the right side was divided by the overall total number of swings to both sides to obtain right-biased swings (%). Subsequently, the brain tissues were removed and washed with saline three times, and then brain tissue was cut into five 2-mm slices. Then, the brain slices were added into a PBS containing 2% TTC and incubated at 37°C for 20 min. After TTC staining, the brain slices were fixed in 4% paraformaldehyde solution for imaging and quantification analysis. The 4-μm sections of brain tissues were obtained and underwent H&E staining, Nissl staining, and TUNEL-Hoechst costaining. The expression levels of GFAP (a marker of astrocytes) and Iba-1 (a marker of microglia) in brain sections of MCAO mice were examined by IHC staining. The internalization of CeO_2@ZIF-8 in the brain tissue of MCAO model mice was also examined by TEM as per the preceding method. The animal studies were approved by the Animal Experimentation Ethics Committee of the Jinan University.

Detection of antioxidant enzymes and inflammatory factor in brain tissue

The contents of MDA (an important product of membrane lipid peroxidation) and antioxidant enzymes of SOD and GSH-Px in the brain tissue of the MCAO mice were examined using the ELISA kits. Briefly, the brain homogenate in the infarct sites was obtained by tissue homogenizer and centrifuged at 12,000 rpm for 10 min to keep the supernatant, and then the protein concentration was examined by bicinchoninic acid assay. Then, the brain homogenates with the same protein concentration in different-treatment MCAO mice were examined to detect the contents of MDA, SOD, and GSH-Px using the ELISA kits according to the specification method. Then, the concentration of inflammatory factors including IL-1β, IL-6, and TNF-α in brain homogenate was also examined using ELISA kits (obtained from Thermo Fisher Scientific) according to the specifications.

In vivo fluorescence imaging of ICG-labeled CeO_2@ZIF-8 in MCAO mice

ICG-labeled nanosystem was synthesized with slight modification of that of CeO_2@ZIF-8. Briefly, 3.5 mg of PVP-CeO_2 was added into 5 ml of 2-methylimidazole (25.6 mM, dissolved in methanol solution) and ICG aqueous solution (10 mg/ml, 1 ml) and stirred for 15 min. Five milliliters of 25.2 mM $Zn(NO_3)_2{\cdot}6H_2O$ methanol solution was then added into the mixed solution to stir for another 20 min at room temperature. The ICG-labeled CeO_2@ZIF-8 was collected by centrifugation and vacuum drying. The ICG-labeled CeO_2@ZIF-8 (0.4 mg/kg) was intravenously injected into C57 MCAO mice, which was then anesthetized and monitored using a fluorescence imaging system (NightOWL II LB 983) at different time points.

Pharmacokinetic study of CeO_2 and CeO_2@ZIF-8

Eight female SD mice (250 to 300 g) were randomly divided into two groups and intravenously injected with CeO_2 and CeO_2@ZIF-8 at the dose of 0.4 mg/kg. Then, blood samples (~1 ml) were collected from the eyes of SD mice at 0, 1, 2, 4, 8, 12, 24, 48, and 72 hours, respectively. The serum samples were obtained by centrifugation and nitrification, and then the content of cerium was determined by ICP-MS. Last, data acquisition and the calculation of related pharmacokinetic parameters were realized by WinNonlin 3.3 software.

Biodistribution of CeO_2@ZIF-8 in the main organs

Eight female SD mice (250 to 300 g) were randomly divided into two groups and intravenously injected with CeO_2 and CeO_2@ZIF-8 at 0.4 mg/kg (injection volume: 1 ml). After 72 hours, the main organs, including heart, liver, spleen, lungs, kidney, and brain, were removed, and the contents of cerium in these organs were examined by ICP-MS.

Toxicity evaluation of CeO_2@ZIF-8 in vivo

The healthy C57 mice (~23 g) were used to evaluate the toxicity of CeO_2@ZIF-8 in vivo. The mice were randomly divided into three groups: control and CeO_2@ZIF-8 (0.4 and 0.8 mg/kg) (six mice per group). CeO_2@ZIF-8 was dispersed in saline solution and injected at the caudal vein (injection volume: 100 μl). After 2 weeks, serum samples were collected for hematological analysis, including blood glucose (GLU), cholesterol (CHOL), triglyceride (TG), high-density lipoprotein cholesterol (HDL-CH), low-density lipoprotein cholesterol (LDL-CH), alanine aminotransferase (ALT), aspartate transaminase (AST), total protein (TP), albumin (ALB), globulin (GLOB), albumin/globulin (ALB/GLOB), uric acid (UA), creatinine (Cr), creatine kinase (CK), and lactate dehydrogenase (LDH). Meanwhile, the main organs (including heart, spleen, lung, liver, kidney, and brain) were collected for H&E staining and pathological analysis.

Statistical analysis

Experiments were repeated at least in triplicate in this study, and all data were expressed as means ± SD. Multiple-group comparison and statistical analysis were performed using SPSS statistical program version 25 (IBM Corp., Armonk, NY) and one-way analysis of variance

(ANOVA). Differences of $^{*}P < 0.05$, $^{**}P < 0.01$, and $^{***}P < 0.001$ were considered statistically significant.

SUPPLEMENTARY MATERIALS

Supplementary material for this article is available at http://advances.sciencemag.org/cgi/content/full/6/12/eaay9751/DC1

Fig. S1. Characterization of the synthetic nanomaterials.
Fig. S2. Examination of free radical scavenging activity of the nanotherapeutics.
Fig. S3. N_2 adsorption-desorption isotherm and pore property analysis.
Fig. S4. CeO_2@ZIF-8 inhibits cell apoptosis and ROS overproduction induced by t-BOOH.
Fig. S5. Change in cell microstructure and mice body weight.
Fig. S6. Brain protection effects of CeO_2@ZIF-8 in C57 MCAO mice.
Fig. S7. Fluorescence imaging and biodistribution analysis of CeO_2@ZIF-8 in vivo.
Fig. S8. H&E staining of the heart, liver, spleen, lung, and kidney after treatment with CeO_2@ZIF-8 for 3 days in MCAO mice model.
Fig. S9. Toxicity evaluation of CeO_2@ZIF-8 in vivo.
Table S1. Pharmacokinetic parameters of CeO_2 nanopolyhedra and CeO_2@ZIF-8 composite nanomaterials.

View/request a protocol for this paper from *Bio-protocol*.

REFERENCES AND NOTES

1. G. J. Hankey, Stroke. *Lancet.* **389**, 641–654 (2017).
2. G. J. Hankey, Secondary prevention of recurrent stroke. *Stroke* **36**, 218–221 (2005).
3. S. S. Andrabi, M. Ali, H. Tabassum, S. Parveen, S. Parvez, Pramipexole prevents ischemic cell death via mitochondrial pathways in ischemic stroke. *Dis. Models Mech.* **12**, dmm033860 (2019).
4. C. L. Allen, U. Bayraktutan, Oxidative stress and its role in the pathogenesis of ischaemic stroke. *Int. J. Stroke* **4**, 461–470 (2009).
5. Y. Fu, Q. Liu, J. Anrather, F. D. Shi, Immune interventions in stroke. *Nat. Rev. Neurol.* **11**, 524–535 (2015).
6. A. Flemming, Calming inflammation to prevent stroke damage. *Nat. Rev. Immunol.* **19**, 473 (2019).
7. S. Matsumoto, M. Murozono, M. Kanazawa, T. Nara, T. Ozawa, Y. Watanabe, Edaravone and cyclosporine a as neuroprotective agents for acute ischemic stroke. *Acute Med. Surg.* **5**, 213–221 (2018).
8. X. R. Lee, G. L. Xiang, Effects of edaravone, the free radical scavenger, on outcomes in acute cerebral infarction patients treated with ultra-early thrombolysis of recombinant tissue plasminogen activator. *Clin. Neurol. Neurosurg.* **167**, 157–161 (2018).
9. S. Bhattacharjee, B. Jun, L. Belayev, J. Heap, M.-A. Kautzmann, A. Obenaus, H. Menghani, S. J. Marcell, L. Khoutorova, R. Yang, N. A. Petasis, N. G. Bazan, Elovanoids are a novel class of homeostatic lipid mediators that protect neural cell integrity upon injury. *Sci. Adv.* **3**, e1700735 (2017).
10. J. Wu, X. Wang, Q. Wang, Z. Lou, S. Li, Y. Zhu, L. Qin, H. Wei, Nanomaterials with enzyme-like characteristics (nanozymes): Next-generation artificial enzymes (II). *Chem. Soc. Rev.* **48**, 1004–1076 (2019).
11. D. Jiang, D. Ni, Z. T. Rosenkrans, P. Huang, X. Yan, W. Cai, Nanozyme: New horizons for responsive biomedical applications. *Chem. Soc. Rev.* **48**, 3683–3704 (2019).
12. J. Wang, J. Yu, Y. Zhang, X. Zhang, A. R. Kahkoska, G. Chen, Z. Wang, W. Sun, L. Cai, Z. Chen, C. Qian, Q. Shen, A. Khademhosseini, J. B. Buse, Z. Gu, Charge-switchable polymeric complex for glucose-responsive insulin delivery in mice and pigs. *Sci. Adv.* **5**, eaaw4357 (2019).
13. J. Feng, S. Lepetre-Mouelhi, A. Gautier, S. Mura, C. Cailleau, F. Coudore, M. Hamon, P. Couvreur, A new painkiller nanomedicine to bypass the blood-brain barrier and the use of morphine. *Sci. Adv.* **5**, eaau5148 (2019).
14. Y. Liu, K. Ai, X. Ji, D. Askhatova, R. Du, L. Lu, J. Shi, Comprehensive insights into the multi-antioxidative mechanisms of melanin nanoparticles and their application to protect brain from injury in ischemic stroke. *J. Am. Chem. Soc.* **139**, 856–862 (2017).
15. J. Kim, H. Y. Kim, S. Y. Song, S.-H. Go, H. S. Sohn, S. Baik, M. Soh, K. Kim, D. Kim, H.-C. Kim, N. Lee, B.-S. Kim, T. Hyeon, Synergistic oxygen generation and reactive oxygen species scavenging by manganese ferrite/ceria co-decorated nanoparticles for rheumatoid arthritis treatment. *ACS Nano* **13**, 3206–3217 (2019).
16. D. Kim, H. J. Kwon, T. Hyeon, Magnetite/ceria nanoparticle assemblies for extracorporeal cleansing of amyloid-beta in Alzheimer's disease. *Adv. Mater.* **31**, e1807965 (2019).
17. W. Tao, N. Kong, X. Ji, Y. Zhang, A. Sharma, J. Ouyang, B. Qi, J. Wang, N. Xie, C. Kang, H. Zhang, O. C. Farokhzad, J. S. Kim, Emerging two-dimensional monoelemental materials (Xenes) for biomedical applications. *Chem. Soc. Rev.* **48**, 2891–2912 (2019).
18. X. Ji, Y. Kang, J. Ouyang, Y. Chen, D. Artzi, X. Zeng, Y. Xiao, C. Feng, B. Qi, N. Y. Kim, P. E. Saw, N. Kong, O. C. Farokhzad, W. Tao, Synthesis of ultrathin biotite nanosheets as an intelligent theranostic platform for combination cancer therapy. *Adv. Sci.* **6**, 1901211 (2019).
19. H. J. Kwon, D. Kim, K. Seo, Y. G. Kim, S. I. Han, T. Kang, M. Soh, T. Hyeon, Ceria nanoparticle systems for selective scavenging of mitochondrial, intracellular, and extracellular reactive oxygen species in parkinson's disease. *Angew. Chem. Int. Ed.* **57**, 9408–9412 (2018).
20. C. Xu, X. Qu, Cerium oxide nanoparticle: A remarkably versatile rare earth nanomaterial for biological applications. *NPG Asia Mater.* **6**, e90 (2014).
21. C. K. Kim, T. Kim, I.-Y. Choi, M. Soh, D. Kim, Y.-J. Kim, H. Jang, H.-S. Yang, J. Y. Kim, H.-K. Park, S. P. Park, S. Park, T. Yu, B.-W. Yoon, S.-H. Lee, T. Hyeon, Ceria nanoparticles that can protect against ischemic stroke. *Angew. Chem. Int. Ed.* **51**, 11039–11043 (2012).
22. Q. Bao, P. Hu, Y. Xu, T. Cheng, C. Wei, L. Pan, J. Shi, simultaneous blood-brain barrier crossing and protection for stroke treatment based on edaravone-loaded ceria nanoparticles. *ACS Nano* **12**, 6794–6805 (2018).
23. X. Dong, J. Gao, C. Y. Zhang, C. Hayworth, M. Frank, Z. Wang, Neutrophil membrane-derived nanovesicles alleviate inflammation to protect mouse brain injury from ischemic stroke. *ACS Nano* **13**, 1272–1283 (2019).
24. W. Lv, J. P. Xu, X. Wang, X. Li, Q. Xu, H. Xin, Bioengineered boronic ester modified dextran polymer nanoparticles as reactive oxygen species responsive nanocarrier for ischemic stroke treatment. *ACS Nano* **12**, 5417–5426 (2018).
25. Y. Long, S. Song, J. Li, L. Wu, Q. Wang, Y. Liu, R. Jin, H. Zhang, Pt/CeO_2@MOF Core@Shell nanoreactor for selective hydrogenation of furfural via the channel screening effect. *ACS Catal.* **8**, 8506–8512 (2018).
26. W. Ngwa, Systemic immune effects boost radiotherapy. *Nat. Biomed. Eng.* **2**, 562–563 (2018).
27. H. Zheng, Y. Zhang, L. Liu, W. Wan, P. Guo, A. M. Nystrom, X. Zou, One-pot synthesis of metal organic frameworks with encapsulated target molecules and their applications for controlled drug delivery. *J. Am. Chem. Soc.* **138**, 962–968 (2016).
28. M. Ito, K. Komai, S. Mise-Omata, M. Iizuka-Koga, Y. Noguchi, T. Kondo, R. Sakai, K. Matsuo, T. Nakayama, O. Yoshie, H. Nakatsukasa, S. Chikuma, T. Shichita, A. Yoshimura, Brain regulatory T cells suppress astrogliosis and potentiate neurological recovery. *Nature* **565**, 246–250 (2019).
29. G. Collet, T. Lathion, C. Besnard, C. Piguet, S. Petoud, On-demand degradation of metal-organic framework based on photocleavable dianthracene-based ligand. *J. Am. Chem. Soc.* **140**, 10820–10828 (2018).
30. B. Li, J. G. Ma, P. Cheng, Silica-protection-assisted encapsulation of cu_2o nanocubes into a metal-organic framework (ZIF-8) to provide a composite catalyst. *Angew. Chem. Int. Ed. Engl.* **57**, 6834–6837 (2018).
31. B. Xu, H. Wang, W. Wang, L. Gao, S. Li, X. Pan, H. Wang, H. Yang, X. Meng, Q. Wu, L. Zheng, S. Chen, X. Shi, K. Fan, X. Yan, H. Liu, A single-atom nanozyme for wound disinfection applications. *Angew. Chem. Int. Ed. Engl.* **58**, 4911–4916 (2019).
32. Á. Chamorro, U. Dirnagl, X. Urra, A. M. Planas, Neuroprotection in acute stroke: Targeting excitotoxicity, oxidative and nitrosative stress, and inflammation and infl ammation. *Lancet Neurol.* **15**, 869–881 (2016).
33. Y. Lu, C. Li, Q. Chen, P. Liu, Q. Guo, Y. Zhang, X. Chen, Y. Zhang, W. Zhou, D. Liang, Y. Zhang, T. Sun, W. Lu, C. Jiang, Microthrombus-targeting micelles for neurovascular remodeling and enhanced microcirculatory perfusion in acute ischemic stroke. *Adv. Mater.* **31**, e1808361 (2019).
34. C. Bouchez, A. Devin, Mitochondrial biogenesis and mitochondrial reactive oxygen species (ROS): A complex relationship regulated by the cAMP/PKA signaling pathway. *Cell* **8**, 287 (2019).
35. N. Sadeghian, J. Shadman, A. Moradi, M. Ghasem Golmohammadi, H. Panahpour, Calcitriol protects the blood-brain barrier integrity against ischemic stroke and reduces vasogenic brain edema via antioxidant and antiapoptotic actions in rats. *Brain Res. Bull.* **150**, 281–289 (2019).
36. X. Jiang, A. V. Andjelkovic, L. Zhu, T. Yang, M. V. L. Bennett, J. Chen, R. F. Keep, Y. Shi, Blood-brain barrier dysfunction and recovery after ischemic stroke. *Prog. Neurobiol.* **163–164**, 144–171 (2018).
37. L. Chan, P. Gao, W. Zhou, C. Mei, Y. Huang, X.-F. Yu, P. K. Chu, T. Chen, Sequentially triggered delivery system of black phosphorus quantum dots with surface charge-switching ability for precise tumor radiosensitization. *ACS Nano* **12**, 12401–12415 (2018).
38. Y. Li, X. L. Li, Y.-S. Wong, T. Chen, H. Zhang, C. Liu, W. Zheng, The reversal of cisplatin-induced nephrotoxicity by selenium nanoparticles functionalized with 11-mercapto-1-undecanol by inhibition of ROS-mediated apoptosis. *Biomaterials* **32**, 9068–9076 (2011).
39. T. Chen, Y.-S. Wong, In vitro antioxidant and antiproliferative activities of selenium-containing phycocyanin from selenium-enriched spirulina platensis. *J. Agr. Food Chem.* **56**, 4352–4358 (2008).

Acknowledgments

Funding: This work was supported by the Natural Science Foundation of China (21877049 and 21701051), Fundamental Research Funds for the Central Universities, Natural Science Foundation of Guangdong Province (2017A030313051), China

Postdoctoral Science Foundation (2016M600705), Major Program for Tackling Key Problems of Industrial Technology in Guangzhou (201902020013), and Dedicated Fund for Promoting High-Quality Marine Economic Development in Guangdong Province (GDOE-2019-A31). **Author contributions:** L.H., G.H., and T.C. conceived and designed the experiments. L.H., G.H., and H.L. performed the experiments. L.H., H.L., and C.S. collected and analyzed the data. L.H., G.H., and X.L. took part in animal experiments. C.S. and H.L. took part in discussions. T.C. supervised the project. L.H., G.H., and T.C. wrote the manuscript. All authors discussed the results and commented on the manuscript. **Competing interests:** The authors declare that they have no competing interests. **Data and materials availability:** All data needed to evaluate the conclusions in the paper are present in the paper and/or the Supplementary Materials. Additional data related to this paper may be requested from the authors.

Submitted 2 August 2019
Accepted 20 December 2019
Published 18 March 2020
10.1126/sciadv.aay9751

Citation: L. He, G. Huang, H. Liu, C. Sang, X. Liu, T. Chen, Highly bioactive zeolitic imidazolate framework-8–capped nanotherapeutics for efficient reversal of reperfusion-induced injury in ischemic stroke. *Sci. Adv.* **6**, eaay9751 (2020).